






Article

Synthesis and Characterization of Iron–Sillenite for Application as an XRD/MRI Dual-Contrast Agent

Diana Vistorskaja ¹, Jen-Chang Yang ², Yu-Tzu Wu ², Liang-Yu Chang ², Po-Wen Lu ^{3,4}, Aleksej Zarkov ¹, Inga Grigoraviciute ¹ and Aivaras Kareiva ^{1,*}

- ¹ Institute of Chemistry, Vilnius University, Naugarduko St. 24, 03225 Vilnius, Lithuania; diana.vistorskaja@chgf.vu.lt (D.V.); aleksej.zarkov@chf.vu.lt (A.Z.); inga.grigoraviciute@chf.vu.lt (I.G.)
- ² Graduate Institute of Nanomedicine and Medical Engineering, Taipei Medical University, No. 301, Yuantong Road, Zhonghe District, New Taipei City 235603, Taiwan; yang820065@tmu.edu.tw (J.-C.Y.); woodya228@gmail.com (Y.-T.W.); alex627324@gmail.com (L.-Y.C.)
- ³ Graduate Institute of Biomedical Materials and Tissue Engineering, College of Biomedical Engineering, Taipei Medical University, Taipei 11052, Taiwan; d825110006@tmu.edu.tw
- ⁴ Division of Gastroenterology and Hepatology, Department of Internal Medicine, Shuang Ho Hospital, Taipei Medical University, Zhongzheng Road, Zhonghe, Taipei 23561, Taiwan
- * Correspondence: aivaras.kareiva@chgf.vu.lt

Abstract: In the present work, iron–sillenite ($\text{Bi}_{25}\text{FeO}_{40}$) was synthesized using a simple solid-state reaction method and characterized. The effects of the synthesis conditions on the phase purity of $\text{Bi}_2\text{O}_3/\text{Fe}_3\text{O}_4$, morphological features, and possible application as an XRD/MRI dual-contrast agent were investigated. For the synthesis, the stoichiometric amounts of Bi_2O_3 and Fe_3O_4 were mixed and subsequently milled in a planetary ball mill for 10 min with a speed of 300 rpm. The milled mixture was calcined at various temperatures (550 °C, 700 °C, 750 °C, 800 °C, and 850 °C) for 1 h in air at a heating rate of 5 °C/min. For phase identification, powder X-ray diffraction (XRD) analysis was performed and infrared (FTIR) spectra were recorded. The surface morphology of synthesized samples was studied by field-emission scanning electron microscopy (FE-SEM). For the radiopacity measurements, iron–sillenite specimens were synthesized at different temperatures and mixed with different amounts of BaSO_4 and Laponite solution. It was demonstrated that iron–sillenite $\text{Bi}_{25}\text{FeO}_{40}$ possessed sufficient radiopacity and could be a potential candidate to meet the requirements of its application as an XRD/MRI dual-contrast agent.

Keywords: iron–sillenite; $\text{Bi}_{25}\text{FeO}_{40}$; solid-state reaction synthesis; radiopacity



Citation: Vistorskaja, D.; Yang, J.-C.; Wu, Y.-T.; Chang, L.-Y.; Lu, P.-W.; Zarkov, A.; Grigoraviciute, I.; Kareiva, A. Synthesis and Characterization of Iron–Sillenite for Application as an XRD/MRI Dual-Contrast Agent. *Crystals* **2024**, *14*, 706. <https://doi.org/10.3390/cryst14080706>

Academic Editor: Andrey Prokofiev

Received: 22 June 2024

Revised: 23 July 2024

Accepted: 1 August 2024

Published: 5 August 2024



Copyright: © 2024 by the authors. Licensee MDPI, Basel, Switzerland. This article is an open access article distributed under the terms and conditions of the Creative Commons Attribution (CC BY) license (<https://creativecommons.org/licenses/by/4.0/>).

1. Introduction

The development of biomedical imaging techniques like X-ray, computed tomography (CT), magnetic resonance imaging (MRI), positron emission tomography (PET), digital mammography (DM), optical imaging (OI), and ultrasound (US) is of great importance to obtain comprehensive information about tissues and organs [1]. Currently, various multimodal-contrast-based agents imaging modalities, such as X-ray/US [2], CT/MRI [3], OI/MRI [4], PET/CT [5], and PET/MRI [6], are successfully applied to obtain high sensitivity and anatomic resolution in clinical diseases diagnosis.

Magnetic resonance imaging (MRI) provides detailed images of brain, spine, joint, and soft-tissue examinations [7]. Iron oxide nanoparticles like Fe_2O_3 , with their inherent magnetism, biocompatibility, and flexibility of engineering, are ideal candidates for MRI and multimodal imaging [8]. Radiopacity is essential for tracking medical devices in X-ray images during procedures. Bismuth oxide (Bi_2O_3) is widely used for dental filling materials due to its acceptable radiopacity to distinguish it from surrounding anatomic structures [9]. A modified $\text{Bi}_2\text{O}_3/\text{ZrO}_2$ radiopacifier was proposed to improve its biocompatibility [10].

Solid-state synthesis has been conventionally used for inorganic compounds, but there is also a growing interest in solvent-free organic synthesis to design new materials [11].

Solid-state reaction syntheses offer several advantages related to their adaptability with multi-elemental phases from a mixture of solid starting materials in direct reactions at high temperatures [12].

Sillenite-type members of the bismuth ferrite family have demonstrated outstanding potential as novel photocatalysts in environmental remediation [13]. It was shown recently that iron–sillenite ($\text{Bi}_{25}\text{FeO}_{40}$) can be successfully used as a supercapacitor candidate and for dye-sensitized solar cells [14]. The structural, optical, dielectric, catalytic, and magnetic properties of $\text{Bi}_{25}\text{FeO}_{40}$ can be controlled by changing particle size, by doping with other metals, or by developing composites [15,16]. For example, with increasing Cr concentration in Cr-doped $\text{Bi}_{25}\text{FeO}_{40}$ ($\text{Bi}_{25}\text{Fe}_{1-x}\text{Cr}_x\text{O}_{40}$, $x = 0-0.5$), the shape of particles has changed from microcubes ($x = 0$) to microspheres ($x = 0.3$) owing to the lattice expansion [17]. The Sb-doped $\text{Bi}_{25}\text{FeO}_{40}$ showed significant electrocatalytic activity [18]. The composite with SiO_2 ($\text{Bi}_{25}\text{FeO}_{40}/\text{SiO}_2$) had quite different microstructural, optical, and magnetic properties and an improved specific absorption rate of the nanoparticles [19].

Firstly, iron–sillenite was isolated as the impurity phase during the preparation of perovskite BiFeO_3 (BFO) or its derivatives [20]. For example, during the synthesis of $\text{Bi}_{1-x}\text{La}_x\text{FeO}_3$ by the co-precipitation method, single-phase BFO phase formed when $x = 0.3$. With an increasing amount of lanthanum, the impurity $\text{Bi}_{25}\text{FeO}_{40}$ phase was detected in the synthesis products [21]. When the sol–gel–combustion synthesis method was applied for preparation of BFO, the pure phase was obtained only at a low heating rate and annealing temperatures between 500 °C and 600 °C. It was determined that, above 600 °C, the BiFeO_3 gradually decomposed to $\text{Bi}_{25}\text{FeO}_{40}$ and $\text{Bi}_2\text{Fe}_4\text{O}_9$ [22]. Goldman et al. [23] also observed that sillenite formed as intermediate product during synthesis of BFO using a hydrothermal approach. Similar results have been published by Sansom et al. [24] and Yang et al. [25]. Later, the monophasic $\text{Bi}_{25}\text{FeO}_{40}$ was synthesized using hydrothermal [26–28], combustion [26], molten salts [29], and mechanical [30] synthesis methods. The final products obtained by different synthesis approaches showed different surface morphology and physical properties.

Different composites with $\text{Bi}_{25}\text{FeO}_{40}$ have been also synthesized and investigated. The $\text{Bi}_{25}\text{FeO}_{40}$ –graphene composite photocatalyst exhibited higher catalytic activity, was superparamagnetic, and can be readily recovered in an external magnetic field [31]. The $\text{Bi}/\text{Bi}_{25}\text{FeO}_{40}$ –C even exhibited higher catalytic efficiency [32]. It was demonstrated that the sillenite–graphene oxide nanocomposite is promising for improving the magnetic and optical properties for potential technological applications [33,34]. Silver phosphate/sillenite bismuth ferrite/graphene oxide ($\text{Ag}_3\text{PO}_4/\text{Bi}_{25}\text{FeO}_{40}/\text{GO}$) nanocomposite has been successfully fabricated as well [35]. In the work by [36], a $\text{Bi}_{25}\text{FeO}_{40}$ – Fe_3O_4 – Fe_2O_3 composite was prepared directly through the solid-state reaction process. The results of the investigation indicated that these composite samples have photocatalytic properties which can be easily recycled by magnetic separation.

The heterojunction nanostructures of bismuth iron oxides showed enhanced photocatalytic and other properties. A $\text{Bi}_{25}\text{FeO}_{40}/\text{Bi}_2\text{Fe}_4\text{O}_9$ photocatalyst has been synthesized and evaluated as a visible-light responsive catalyst for the degradation of Rhodamine B [37]. A heterojunction-type charge transfer mechanism interpreting the enhanced photocatalytic activities was proposed and discussed in this study. The strategies of $\text{BiFeO}_3/\text{Bi}_{25}\text{FeO}_{40}$ heterojunction construction, temperature, and morphology controlling and Fe^{3+} doping allowed precise regulation of the band gap structure of bismuth ferrite [38,39]. These findings promoted the application of BiFeO_3 in photocatalytic and other redox reactions.

Magnetic resonance imaging (MRI) has become one of the most prominent and widely adapted diagnostic imaging methods in the realm of clinical practice and biomedical research because of its superior spatial resolution and 3D tomographic images with anatomical details. To date, only a few nanosystems have been investigated as T1 MRI-CT dual-contrast agents. The summarized results suggest that D-glucuronic acid-coated $\text{Gd}(\text{IO}_3)_3$ center dot [40], low-magnetization magnetite nanocubes [41], Eu-doped iron oxide nanoparticles [42], functionalized Fe_3O_4 composites [43], or ($\text{Fe}_3\text{O}_4/\gamma\text{-Fe}_2\text{O}_3$) nanoparticles coated

by gadolinium–diethylenetriaminepentaacetic acid [44] could be potential T1 MRI-CT dual-contrast reagents. However, these dual-contrast agents have a relatively low sensitivity compared with other imaging methods. Moreover, most of them suffer from low relaxation and contrast efficiency, which hampers their application in clinical diagnosis.

In this study, we aim to fill this gap. Iron–sillenite ($\text{Bi}_{25}\text{FeO}_{40}$) was synthesized using a simple solid-state reaction method and characterized. The effects of the synthesis conditions on the phase purity of $\text{Bi}_2\text{O}_3/\text{Fe}_3\text{O}_4$, morphological features, and possible application as an XRD/MRI dual-contrast agent were investigated.

2. Materials and Methods

2.1. Synthesis

Iron–sillenite ($\text{Bi}_{25}\text{FeO}_{40}$) was synthesized using a simple solid-state reaction method. Stoichiometric amounts of Bi_2O_3 (Alfa Aesar, Haverhill MA, USA, 99.9%) and Fe_3O_4 (Sigma-Aldrich, St. Louis, MO, USA, 97.0%) were mixed and subsequently milled in a planetary ball mill for 10 min with a speed of 300 rpm. Ball milling was performed using a bench-top planetary ball mill (Retsch PM100, Haan, Germany). The conditions involved loading a 10 g sample into a 50 mL alumina grinding jar and adding 10 alumina grinding balls (each with a diameter of 10 mm). The milled mixture was calcined at various temperatures (550 °C, 700 °C, 750 °C, 800 °C, and 850 °C) for 1 h in air at a heating rate of 5 °C/min. Finally, the synthesized products were ground in an agate mortar. A simplified scheme of the synthesis route of iron–sillenite is presented in Figure 1.



Figure 1. Solid-state reaction synthesis of $\text{Bi}_{25}\text{FeO}_{40}$.

2.2. Characterization

For phase identification at ambient temperature, the XRD data were collected at 20–70° 2θ range (step width of 0.2°, scan speed 3.33°/min) using Ni-filtered $\text{Cu K}\alpha_1$ ($\lambda = 1.54184 \text{ \AA}$) radiation on a Bruker D2 PHASER diffractometer. Infrared (FTIR) spectra were recorded in the range of 4000–400 cm^{-1} employing a Bruker ALPHA ATR spectrometer. In order to study the morphology of the samples, a field-emission scanning electron microscope (FE-SEM) Hitachi SU-70 (Tokyo, Japan) was used. The radiopacity of samples was measured using a dental X-ray system (VX-65, Shanghai, China) and X-ray images recorded by an occlusal radiographic imaging plate (Kodak CR, Los Angeles, CA, USA). The mean grayscale values of each step of the aluminum step wedge (from 2 to 16 mm in 2 mm increments) and the specimens were measured and analyzed using imaging processing software ImageJ 1.39f (Wayne Rasband). For the radiopacity measurements, iron–sillenite samples were synthesized at different temperatures and mixed with different amounts of BaSO_4 (Alfa Aesar, Haverhill MA, USA, 99.0%) and Laponite solution (Sigma-Aldrich, St. Louis, MO, USA, $\text{LiMgNaO}_6\text{Si}_2$, 1% solution).

3. Results and Discussion

The XRD patterns of $\text{Bi}_{25}\text{FeO}_{40}$ synthesis products obtained at 700 °C, 750 °C, and 800 °C are presented in Figure 2.

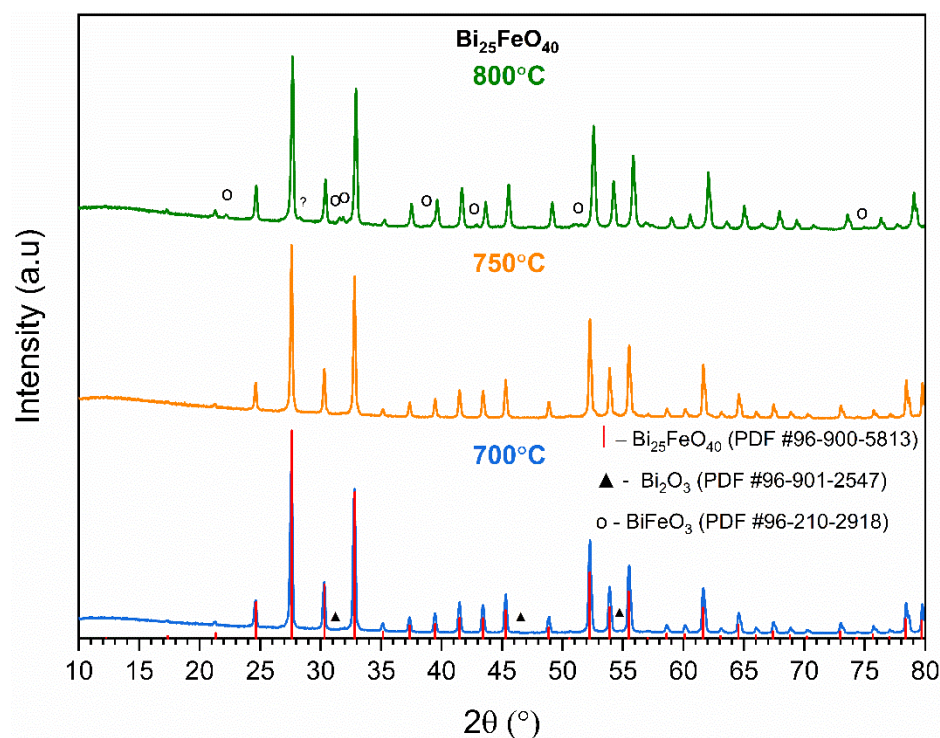


Figure 2. XRD patterns of $\text{Bi}_{25}\text{FeO}_{40}$ synthesis products obtained at 700 °C, 750 °C, and 800 °C. Vertical lines represent the standard XRD pattern of $\text{Bi}_{25}\text{FeO}_{40}$.

As can be seen from the XRD diffraction patterns of synthesis products obtained at 750 °C, all the peaks match very well with the standard XRD data of $\text{Bi}_{25}\text{FeO}_{40}$ (PDF #96-900-5813). Also, iron-sillenite was the main crystalline phase in the products annealed at slightly lower or higher temperatures. However, unreacted Bi_2O_3 was determined in the XRD pattern of the sample obtained at 700 °C, while perovskite BiFeO_3 and some unidentified phase formed at 800 °C. Evidently, the solid-state reaction performed at 550 °C was not complete and the reaction mixture annealed at 850 °C was already melted with the formation of multiphasic product (see Figure S1). Thus, the apparently optimal temperature for solid-state reaction synthesis of monophasic $\text{Bi}_{25}\text{FeO}_{40}$ is 750 °C.

FTIR spectra of the products obtained at 700 °C, 750 °C, and 800 °C are presented in Figure 3. The FTIR range of 1250–400 cm^{-1} was chosen as representative since the main bands attributed to $\text{Bi}_{25}\text{FeO}_{40}$ synthesis products can be observed in this region. As can be seen, only stretching modes of metal–oxygen (M–O) vibrations can be observed at approximately 820 cm^{-1} , and in the range of 625–430 cm^{-1} in the FTIR spectra of all three samples. These absorption bands correspond to the vibration of the Fe–O, Bi–O, or Bi–O–Fe bonds in the crystalline lattice of $\text{Bi}_{25}\text{FeO}_{40}$ [45–48]. Such results are in a good agreement with the XRD data.

The morphology of the $\text{Bi}_{25}\text{FeO}_{40}$ synthesis products obtained at 700 °C, 750 °C, and 800 °C was almost identical. However, the samples sintered at 550 °C and 850 °C showed quite different morphological features. The SEM micrographs of the representative samples are shown in Figure 4.

As can be seen, the particle shape varied from plate-like, spherical to multishaped and flower-like structures by changing the synthesis temperature from 550 °C to 850 °C. The samples fabricated at 700–800 °C were composed of spherical shapes and grew into each other's particles at 1–2 μm in size. It is worth noting that the narrow particle size distribution was achieved even though the synthesis was performed by the solid-state reaction method. The results of EDX analysis confirmed the molar ratio of Bi and Fe in synthesized $\text{Bi}_{25}\text{FeO}_{40}$. The EDX spectrum and color mapping, along with the SEM image of the representative sample, is provided in Figure S2.

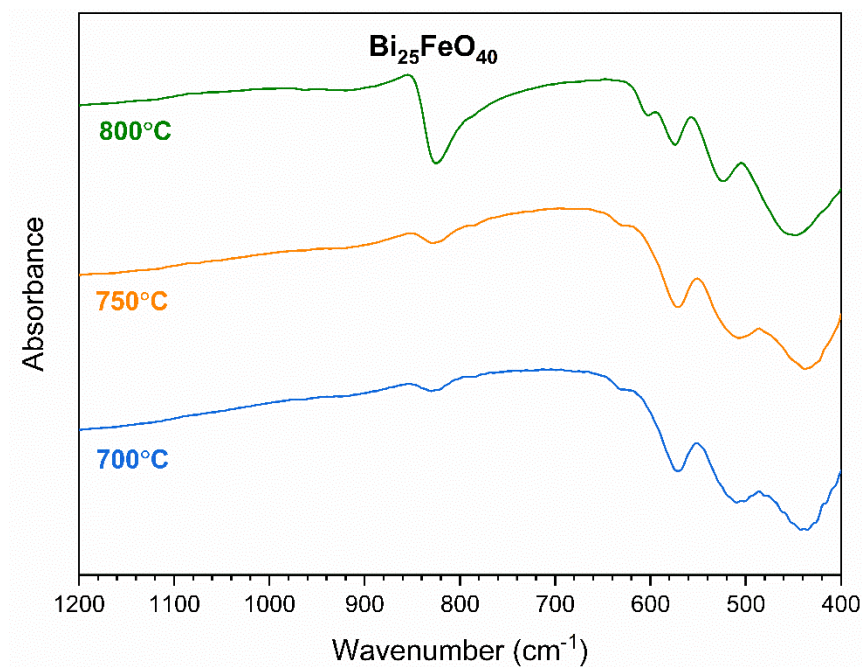


Figure 3. FTIR spectra of $\text{Bi}_{25}\text{FeO}_{40}$ synthesis products obtained at 700 °C, 750 °C, and 800 °C.

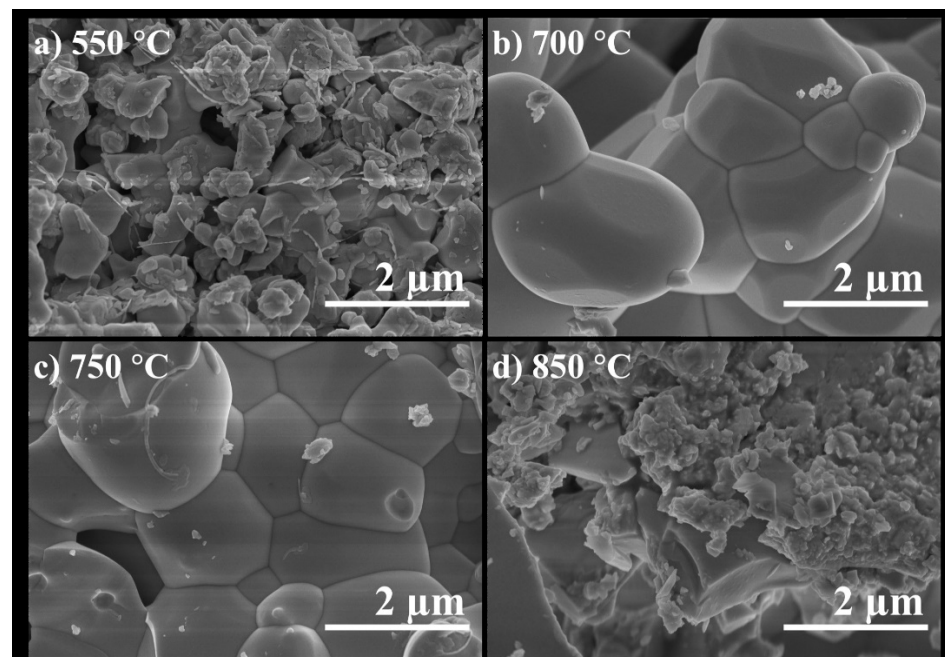


Figure 4. SEM micrographs of $\text{Bi}_{25}\text{FeO}_{40}$ synthesis products obtained at different temperatures (a) 550 °C; (b) 700 °C; (c) 750 °C; (d) 850 °C.

Radiopacity is a key factor to verify the efficiency of a radiocontrast agent in imaging [49]. The synthesized samples were also characterized by the radiopacity measurements. For the radiopacity measurements, the $\text{Bi}_{25}\text{FeO}_{40}$ synthesized at 750 °C was mixed with different amount of BaSO_4 and Laponite solution. Initially, the control reference samples were prepared from BaSO_4 and Laponite using different ratios of constituents (see Table 1). The stability of the reference samples was checked visually. It is evident from digital photos presented in Figure 5 that the color of different mixtures of BaSO_4 and Laponite were stable for 12 h. The aluminum step wedge (99.5% Al) was used as an internal standard for measuring the equivalent radiopacity of different materials [50,51]. The results of

the radiopacity of reference samples with composition presented in Table 1 are shown in Table 2. The grayscale value corresponds to the attenuation of the material. The measured grayscale value for each reference composition and aluminum corresponds to the amount of attenuation. The regression parameter R^2 for the investigated systems varied in the range of 0.9948–0.9977.

Table 1. The reference samples used for the radiopacity measurements.

Name of Control Sample	m(BaSO ₄), G	m(Laponite Solution), G
A1	0.1	0.9
B1	0.2	0.8
C1	0.3	0.7
A2	0.2	1.8
B2	0.4	1.6
C2	0.6	1.4

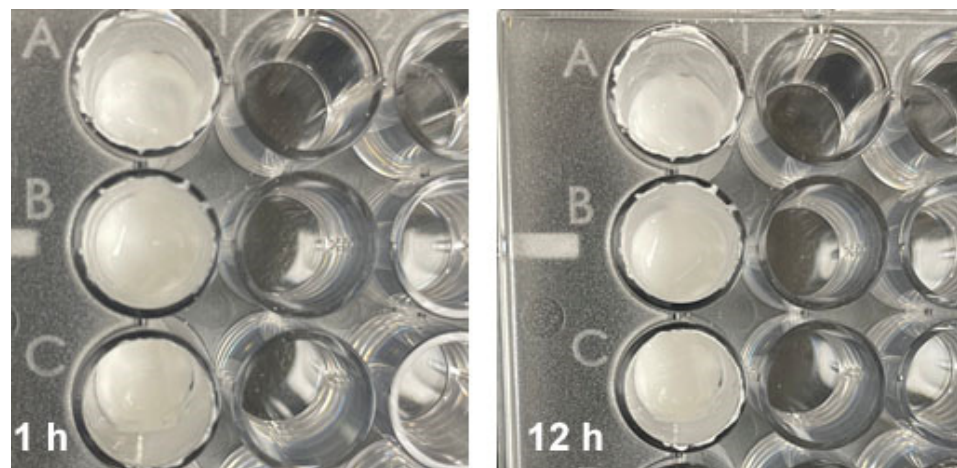


Figure 5. Photos of reference samples prepared after 1 h and 12 h showing the stability of prepared reference materials.

Table 2. The radiopacity of reference samples.

Name of Control Sample	Grayscale Value	mm Al
A1	10.773	0.355
B1	84.596	3.387
C1	142.910	2.922
A2	53.893	0.681
B2	83.008	4.257
C2	159.511	5.092

As can be seen from Table 2, the radiopacity values for the system A2, B2, and C2 were higher in comparison with A1, B1, and C1. Therefore, the BaSO₄ and Laponite samples from series A2, B2, and C2 were selected for the investigation of the radiopacity of the iron–sillenite sample synthesized at 750 °C using a solid-state reaction method. These samples are marked A3, B3, and C3, respectively. Again, the samples with iron–sillenite showed excellent stability over time (see Figure 6).

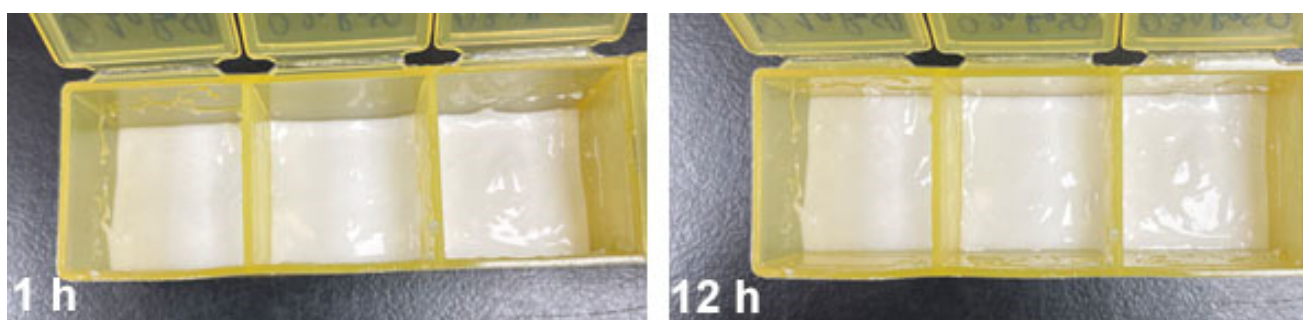


Figure 6. Photos of samples with iron–sillenite prepared after 1 h and 12 h.

Visual examination of the radiographic images (Figure 7) revealed that all three A3, B3, and C3 specimens were homogeneous [51,52]. Evidently, the samples are free of radiolucent and radiopaque inclusions.

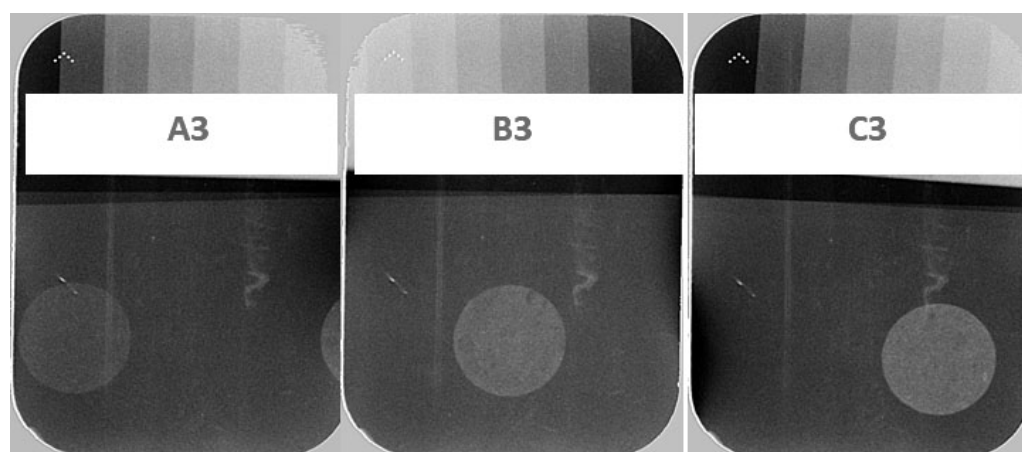


Figure 7. Radiographs of iron–sillenite $\text{Bi}_{25}\text{FeO}_{40}$ specimens mixed with BaSO_4 and Laponite.

To quantify the radiopacity, an Al wedge was again placed beside the iron–sillenite material during X-ray image acquisition and the grayscale values of the material of interest along with the step wedge were digitally analyzed. The radiopacity of the specimen was then referenced to the thickness of aluminum and expressed as the equivalent aluminum thickness (mm Al) [53]. The calibration curves were plotted using best-fit logarithmic regression analysis for the selected data. The equivalent in thickness of aluminum for each material was calculated from the calibration curves. The average magnitude of the mean regression residuals was 0.040 mm of aluminum and the maximum regression residual was 0.125 mm of aluminum. The residuals were random with respect to radiopacity, indicating that no major non-linearity was present. The results' radiopacity of iron–sillenite $\text{Bi}_{25}\text{FeO}_{40}$ specimens obtained are presented in Figure 8 and Table 3.

Table 3. The radiopacity of iron–sillenite $\text{Bi}_{25}\text{FeO}_{40}$ specimens.

Name of Control Sample	Investigated Samples		Background		Iron–Sillenite mm Al
	Grayscale Value	mm Al	Grayscale Value	mm Al	
A3	68.406 ± 6.534	2.279	60.143 ± 6.382	1.920	0.359
B3	102.346 ± 7.559	3.379	75.137 ± 6.242	2.274	1.105
C3	100.070 ± 7.654	3.790	60.731 ± 6.652	1.967	1.823

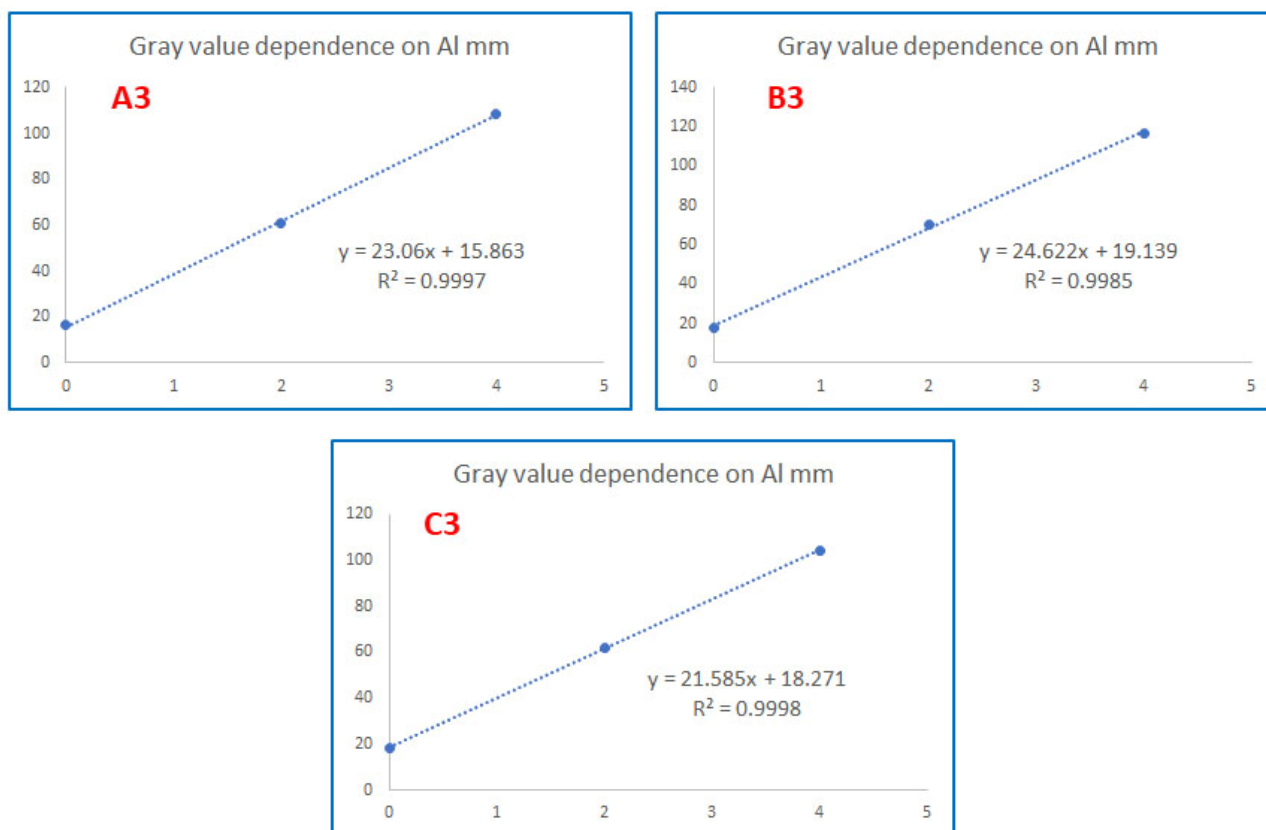


Figure 8. Grayscale value dependence on Al mm.

In conclusion, the radiopacities of the tested B3 and C3 materials were greater than 0.5 mm and greater than the same thickness of aluminum. Therefore, the solid-state reaction-derived iron–sillenite $\text{Bi}_{25}\text{FeO}_{40}$ possessed sufficient radiopacity and could be a potential candidate to meet the requirements of its application as an XRD/MRI dual-contrast agent.

4. Conclusions

In this study, iron–sillenite ($\text{Bi}_{25}\text{FeO}_{40}$) was synthesized using a simple solid-state reaction method and characterized. The effects of the synthesis conditions on the phase purity of $\text{Bi}_2\text{O}_3/\text{Fe}_3\text{O}_4$, morphological features, and possible application as an XRD/MRI dual-contrast agent were investigated. To obtain the iron–sillenite phase, the mixture of starting reagents was calcined at various temperatures (550 °C, 700 °C, 800 °C, and 850 °C). The powder XRD analysis data showed that the synthesis product obtained at 750 °C was monophasic $\text{Bi}_{25}\text{FeO}_{40}$. Also, iron–sillenite was the main crystalline phase in the products annealed at slightly lower or higher temperatures (700 °C and 800 °C, respectively). However, unreacted Bi_2O_3 was determined in the XRD pattern of the sample obtained at 700 °C, while perovskite BiFeO_3 and some unidentified phase formed at 800 °C. Evidently, the solid-state reaction performed at 550 °C was not complete and the reaction mixture annealed at 850 °C was already melted with the formation of multiphasic product. FTIR spectroscopy results were in a good agreement with the XRD data. The samples fabricated at 700–800 °C were composed of spherical shapes and grew into each other's particles at 1–2 μm in size. The synthesized samples were also characterized by the radiopacity measurements. For the radiopacity measurements, the $\text{Bi}_{25}\text{FeO}_{40}$ synthesized at 750 °C was mixed with different amount of BaSO_4 and Laponite solution. Visual examination of the radiographic images revealed that the specimens were homogeneous. The radiopacities of the best compositions were greater than 0.5 mm and greater than the same thickness aluminum. Therefore, the solid-state reaction-derived iron–sillenite $\text{Bi}_{25}\text{FeO}_{40}$ possessed

sufficient radiopacity and could be a potential candidate to meet the requirements of its application as an XRD/MRI dual-contrast agent.

Supplementary Materials: The following supporting information can be downloaded at: <https://www.mdpi.com/article/10.3390/cryst14080706/s1>, Figure S1: XRD patterns of Bi₂₅FeO₄₀ synthesis products obtained at 550 and 850 °C along with standard XRD pattern of starting materials; Figure S2: The EDX spectrum (top) and colour mapping along with SEM images (bottom) of Bi₂₅FeO₄₀ synthesis products obtained at 700 °C.

Author Contributions: Conceptualization, J.-C.Y.; methodology, A.K., L.-Y.C. and A.Z., investigation, Y.-T.W., P.-W.L., D.V. and I.G., resources, J.-C.Y. and A.K., data curation, L.-Y.C., Y.-T.W., D.V., I.G. and A.Z., writing—original draft preparation, A.K. and J.-C.Y., writing—review and editing, A.K. and J.-C.Y., supervision, A.K. and J.-C.Y.; funding acquisition, A.K. and J.-C.Y. All authors have read and agreed to the published version of the manuscript.

Funding: This research received funding by NSTC112-2221-E-038-013 from Taipei Medical University and Vilnius University.

Data Availability Statement: The original contributions presented in the study are included in the article/Supplementary Material, further inquiries can be directed to the corresponding authors.

Conflicts of Interest: The authors declare no conflicts of interest.

References

1. Hussain, S.; Mubeen, I.; Ullah, N.; Shahab, S.; Shah, U.D.; Khan, B.A.; Zahoor, M.; Ullah, R.; Khan, F.A.; Sultan, M.A. Modern Diagnostic Imaging Technique Applications and Risk Factors in the Medical Field: A Review. *Biomed. Res. Int.* **2022**, *2022*, 5164970. [[CrossRef](#)] [[PubMed](#)]
2. Aimacana, C.M.C.; Perez, D.A.Q.; Pinto, S.R.; Debut, A.; Attia, M.F.; Santos-Oliveira, R.; Whitehead, D.C.; Terencio, T.; Alexis, F.; Dahoumane, S.A. Polytetrafluoroethylene-like Nanoparticles as a Promising Contrast Agent for Dual Modal Ultrasound and X-ray Bioimaging. *ACS Biomater. Sci. Eng.* **2021**, *7*, 1181–1191. [[CrossRef](#)] [[PubMed](#)]
3. Ventura, M.; Sun, Y.; Rusu, V.; Laverman, P.; Borm, P.; Heerschap, A.; Oosterwijk, E.; Boerman, O.C.; Jansen, J.A.; Walboomers, X.F. Dual contrast agent for computed tomography and magnetic resonance hard tissue imaging. *Tiss. Eng. C Methods* **2013**, *19*, 405–416. [[CrossRef](#)] [[PubMed](#)]
4. Zhu, T.; Ma, X.; Chen, R.; Ge, Z.; Xu, J.; Shen, X.; Jia, L.; Zhou, T.; Luo, Y.; Ma, T. Using fluorescently-labeled magnetic nanocomposites as a dual contrast agent for optical and magnetic resonance imaging. *Biomater. Sci.* **2017**, *5*, 1090–1100. [[CrossRef](#)] [[PubMed](#)]
5. Farwell, M.D.; Pryma, D.A.; Mankoff, D.A. PET/CT imaging in cancer: Current applications and future directions. *Cancer* **2014**, *120*, 3433–3445. [[CrossRef](#)] [[PubMed](#)]
6. Zhang, Y.; García-Gabilondo, M.; Grayston, A.; Feiner, I.V.J.; Anton-Sales, I.; Loiola, R.A.; Llop, J.; Ramos-Cabrer, P.; Barba, I.; Garcia-Dorado, D.; et al. PLGA protein nanocarriers with tailor-made fluorescence/MRI/PET imaging modalities. *Nanoscale* **2020**, *12*, 4988–5002. [[CrossRef](#)] [[PubMed](#)]
7. Westbrook, C.; Talbot, J. *MRI in Practice*; Wiley: New York, NY, USA, 2018; p. 416.
8. El-Hammadi, M.M.; Arias, J.L. Iron oxide-based multifunctional nanoparticulate systems for biomedical applications: A patent review (2008–present). *Expert Opin. Ther. Pat.* **2015**, *25*, 691–709. [[CrossRef](#)] [[PubMed](#)]
9. Hsieh, S.-C.; Teng, N.-C.; Lin, C.-K.; Lee, P.-Y.; Ji, D.-Y.; Chen, C.-C.; Ke, E.-S.; Lee, S.-Y.; Yang, J.-C. A Novel Accelerator for Improving the Handling Properties of Dental Filling Materials. *J. Endod.* **2009**, *35*, 1292–1295. [[CrossRef](#)] [[PubMed](#)]
10. Chen, C.-C.; Hsieh, S.-C.; Teng, N.-C.; Kao, C.-K.; Lee, S.-Y.; Lin, C.-K.; Yang, J.-C. Radiopacity and cytotoxicity of Portland cement containing zirconia doped bismuth oxide radiopacifiers. *J. Endod.* **2014**, *40*, 251–254. [[CrossRef](#)] [[PubMed](#)]
11. Smart, L.E.; Moore, E.A. *Solid State Chemistry: An Introduction*, 4th ed.; Taylor & Francis: Boca Raton, FL, USA, 2012.
12. Kumar, A.; Dutta, S.; Kim, S.; Kwon, T.; Patil, S.S.; Kumari, N.; Jeevanandham, S.; Lee, I.S. Solid-State Reaction Synthesis of Nanoscale Materials: Strategies and Applications. *Chem. Rev.* **2022**, *122*, 12748–12863. [[CrossRef](#)] [[PubMed](#)]
13. Sharmin, F.; Basith, M.A. Simple Low Temperature Technique to Synthesize Sillenite Bismuth Ferrite with Promising Photocatalytic Performance. *ACS Omega* **2022**, *7*, 34901–34911. [[CrossRef](#)] [[PubMed](#)]
14. Kumar, A.M.; Ragavendran, V.; Mayandi, J.; Ramachandran, K.; Jayakumar, K. Influence of PVP on Bi₂₅FeO₄₀ microcubes for Supercapacitors and Dye-Sensitized Solar Cells applications. *J. Mater. Sci. Mater. Electr.* **2022**, *33*, 9512–9524. [[CrossRef](#)]
15. Jebari, H.; Tahiri, N.; Boujnah, M.; El Bounagui, O.; Boudad, L.; Taibi, M.; Ez-Zahraouy, H. Structural, optical, dielectric, and magnetic properties of iron-sillenite Bi₂₅FeO₄₀. *Appl. Phys.* **2022**, *128*, 842. [[CrossRef](#)]
16. Nayak, A.K.; Gopalakrishnan, T. Phase- and Crystal Structure-Controlled Synthesis of Bi₂O₃, Fe₂O₃, and BiFeO₃ Nanomaterials for Energy Storage Devices. *ACS Appl. Nanomater.* **2022**, *5*, 14663–14676. [[CrossRef](#)]

17. Xiong, Z.W.; Cao, L.H. Tailoring morphology, enhancing magnetization and photocatalytic activity via Cr doping in Bi₂₅FeO₄₀. *J. Alloys Compd.* **2019**, *773*, 828–837. [[CrossRef](#)]
18. Zhang, Y.; Cao, S.H.; Liang, C.; Shen, J.M.; Chen, Y.Q.; Feng, Y.C.; Chen, H.; Liu, R.; Jiang, F. Electrocatalytic performance of Sb-modified Bi₂₅FeO₄₀ for nitrogen fixation. *J. Colloid Interf. Sci.* **2021**, *593*, 335–344. [[CrossRef](#)] [[PubMed](#)]
19. Juwita, E.; Sulistiani, F.A.; Darmawan, M.Y.; Istiqomah, N.I.; Suharyadi, E. Microstructural, optical, and magnetic properties and specific absorption rate of bismuth ferrite/SiO₂ nanoparticles. *Mater. Res. Express* **2022**, *9*, 076101. [[CrossRef](#)]
20. Wu, L.; Dong, C.H.; Chen, H.; Yao, J.L.; Jiang, C.J.; Xue, D.S. Hydrothermal Synthesis and Magnetic Properties of Bismuth Ferrites Nanocrystals with Various Morphology. *J. Am. Ceram. Soc.* **2012**, *95*, 3922–3927. [[CrossRef](#)]
21. Yotburut, B.; Yamwong, T.; Thongbai, P.; Maensiri, S. Synthesis and characterization of coprecipitation-prepared La-doped BiFeO₃ nanopowders and their bulk dielectric properties. *Jpn. J. Appl. Phys.* **2014**, *53*, 06JG13. [[CrossRef](#)]
22. Koefenstein, R. Synthesis, phase evolution and properties of phase-pure nanocrystalline BiFeO₃ prepared by a starch-based combustion method. *J. Alloys Compd.* **2014**, *590*, 324–330. [[CrossRef](#)]
23. Goldman, A.R.; Fredricks, J.L.; Estroff, L.A. Exploring reaction pathways in the hydrothermal growth of phase-pure bismuth ferrites. *J. Cryst. Growth* **2017**, *468*, 104–109. [[CrossRef](#)]
24. Sansom, G.; Rattanakam, R.; Jettanasen, J. Effects of Scaling Up on the Phase Evolution of Microcrystalline Bismuth Ferrite during Hydrothermal Process. *E-J. Surf. Sci. Nanotechnol.* **2022**, *20*, 85–89. [[CrossRef](#)]
25. Yang, X.; Xu, G.; Ren, Z.H.; Weng, W.J.; Du, P.Y.; Shen, G.; Han, G.R. Effect of PVA Adding Amount on Phase-Controlled Synthesis and Morphology Evolution of the Bismuth Ferrite by Assisted Hydrothermal Reaction Route. *Rare Met. Mater. Eng.* **2012**, *41*, 247–249.
26. Koefenstein, R.; Buttler, T.; Ebbinghaus, S.G. Investigations on Bi₂₅FeO₄₀ powders synthesized by hydrothermal and combustion-like processes. *J. Solid State Chem.* **2014**, *217*, 50–56. [[CrossRef](#)]
27. Ji, W.D.; Li, M.M.; Zhang, G.; Wang, P. Controlled synthesis of Bi₂₅FeO₄₀ with different morphologies: Growth mechanism and enhanced photo-Fenton catalytic properties. *Dalton Trans.* **2017**, *46*, 10586–10593. [[CrossRef](#)] [[PubMed](#)]
28. Kumar, A.M.; Ragavendran, V.; Mayandi, J.; Ramachandran, K.; Jayakumar, K. Phase dependent electrochemical characteristics of bismuth ferrite: A bifunctional electrocatalyst for Supercapacitors and Dye-Sensitized Solar Cells. *Colloids Surf. A Physicochem. Eng. Asp.* **2023**, *656*, 130529. [[CrossRef](#)]
29. Ren, L.; Lu, S.Y.; Fang, J.Z.; Wu, Y.; Chen, D.Z.; Huang, L.Y.; Chen, Y.F.; Cheng, C.; Liang, Y.; Fang, Z.Q. Enhanced degradation of organic pollutants using Bi₂₅FeO₄₀ microcrystals as an efficient reusable heterogeneous photo-Fenton like catalyst. *Catal. Today* **2017**, *281*, 656–661. [[CrossRef](#)]
30. Zou, W.J.; Dong, J.T.; Ji, M.X.; Wang, B.; Li, Y.J.; Yin, S.; Li, H.M.; Xia, J.X. Synthesis of Bi₂₅FeO₄₀ Nanoparticles with Oxygen Vacancies via Ball Milling for Fenton Oxidation of Tetracycline Hydrochloride and Reduction of Cr(VI). *ACS Appl. Nano Mater.* **2023**, *6*, 4309–4318. [[CrossRef](#)]
31. Sun, A.W.; Chen, H.; Song, C.Y.; Jiang, F.; Wang, X.; Fu, Y.S. Magnetic Bi₂₅FeO₄₀-graphene catalyst and its high visible-light photocatalytic performance. *RSC Adv.* **2013**, *3*, 4332–4340. [[CrossRef](#)]
32. Li, F.H.; Zhou, J.K.; Gao, C.J.; Qiu, H.X.; Gong, Y.L.; Gao, J.H.; Liu, Y.; Gao, J.P. A green method to prepare magnetically recyclable Bi/Bi₂₅FeO₄₀-C nanocomposites for photocatalytic hydrogen generation. *Appl. Surf. Sci.* **2020**, *521*, 146342. [[CrossRef](#)]
33. Jalil, M.A.; Chowdhury, S.S.; Sakib, M.A.; Yousuf, S.M.E.H.; Ashik, E.K.; Firoz, S.H.; Basith, M.A. Temperature-dependent phase transition and comparative investigation on enhanced magnetic and optical properties between sillenite and perovskite bismuth ferrite-rGO nanocomposites. *J. Appl. Phys.* **2017**, *122*, 084902. [[CrossRef](#)]
34. Basith, M.A.; Ahsan, R.; Zarin, I.; Jalil, M.A. Enhanced photocatalytic dye degradation and hydrogen production ability of Bi₂₅FeO₄₀-rGO nanocomposite and mechanism insight. *Sci. Rep.* **2018**, *8*, 11090. [[CrossRef](#)] [[PubMed](#)]
35. Huang, Y.; Zhang, X.Y.; Zhu, G.X.; Gao, Y.; Cheng, Q.F.; Cheng, X.W. Synthesis of silver phosphate/sillenite bismuth ferrite/graphene oxide nanocomposite and its enhanced visible light photocatalytic mechanism. *Separ. Purif. Technol.* **2019**, *215*, 490–499. [[CrossRef](#)]
36. de Gois, M.M.; Araujo, W.P.; da Silva, R.B.; da Luz, G.E.; Soares, J.M. Bi₂₅FeO₄₀-Fe₃O₄-Fe₂O₃ composites: Synthesis, structural characterization, magnetic and UV-visible photocatalytic properties. *J. Alloys Compd.* **2019**, *785*, 598–602. [[CrossRef](#)]
37. Wang, G.M.; Cheng, D.; He, T.C.; Hu, Y.Y.; Deng, Q.R.; Mao, Y.W.; Wang, S.G. Enhanced visible-light responsive photocatalytic activity of Bi₂₅FeO₄₀/Bi₂Fe₄O₉ composites and mechanism investigation. *J. Mater. Sci. Mater. Electron.* **2019**, *30*, 10923–10933. [[CrossRef](#)]
38. Wang, Y.F.; Xu, C.X.; Yan, L.; Li, J. Synthesis of BiFeO₃/Bi₂₅FeO₄₀ heterojunction structure and precise adjustment of forbidden band width. *Mater. Chem. Phys.* **2023**, *305*, 127935. [[CrossRef](#)]
39. Xu, C.X.; Wang, Y.F.; Wang, Q.; Li, J.; Yan, L. Phase transformation and heterojunction nanostructures of bismuth iron oxide. *J. Mater. Sci. Mater. Electron.* **2023**, *34*, 2236. [[CrossRef](#)]
40. Lee, E.J.; Heo, W.C.; Park, J.W.; Chang, Y.; Bae, J.-E.; Chae, K.S.; Kim, T.J.; Park, J.A.; Lee, G.H. D-Glucuronic Acid Coated Gd(IO₃)₃·2H₂O Nanomaterial as a Potential T1 MRI-CT Dual Contrast Agent. *Eur. J. Inorg. Chem.* **2013**, *16*, 2858–2866. [[CrossRef](#)]
41. Sharma, V.K.; Alipour, A.; Soran-Erdem, Z.; Aykut, Z.G.; Demir, H.V. Highly monodisperse low-magnetization magnetite nanocubes as simultaneous T1-T2 MRI contrast agents. *Nanoscale* **2015**, *7*, 10519–10526. [[CrossRef](#)] [[PubMed](#)]
42. Park, J.C.; Lee, G.T.; Kim, H.-K.; Sung, B.; Lee, Y.; Kim, M.; Chang, Y.; Seo, J.H. Surface Design of Eu-Doped Iron Oxide Nanoparticles for Tuning the Magnetic Relaxivity. *ACS Appl. Mater. Interf.* **2018**, *10*, 25080–25089. [[CrossRef](#)] [[PubMed](#)]

43. Illert, P.; Waengler, B.; Waengler, C.; Zoellner, F.; Uhrig, T.; Litau, S.; Pretze, M.; Roeder, T. Functionalizable composite nanoparticles as a dual magnetic resonance imaging/computed tomography contrast agent for medical imaging. *J. Appl. Polym. Sci.* **2019**, *136*, 47571. [[CrossRef](#)]
44. Eguia-Eguia, S.I.; Gildo-Ortiz, L.; Perez-Gonzalez, M.; Tomas, S.A.; Arenas-Alatorre, J.A.; Santoyo-Salazar, J. Magnetic domains orientation in (Fe₃O₄/γ-Fe₂O₃) nanoparticles coated by Gadolinium-diethylenetriaminepentaacetic acid (Gd³⁺-DTPA). *Nano Express* **2021**, *2*, 020019. [[CrossRef](#)]
45. Kun Yang, K.; Peng, H.; Wen, Y.; Li, N. Re-examination of characteristic FTIR spectrum of secondary layer in bilayer oleic acid-coated Fe₃O₄ nanoparticles. *Appl. Surf. Sci.* **2010**, *256*, 3093–3097. [[CrossRef](#)]
46. Husain, S.; Irfansyah, M.; Haryanti, N.H.; Suryajaya, S.; Arjo, S.; Maddu, A. Synthesis and characterization of Fe₃O₄ magnetic nanoparticles from iron ore. *J. Phys. Conf. Ser.* **2019**, *1242*, 012021. [[CrossRef](#)]
47. Li, W. Facile synthesis of monodisperse Bi₂O₃ nanoparticles. *Mater. Chem. Phys.* **2006**, *99*, 174–180. [[CrossRef](#)]
48. Labib, S. Preparation, characterization and photocatalytic properties of doped and undoped Bi₂O₃. *J. Saudi Chem. Soc.* **2017**, *21*, 664–672. [[CrossRef](#)]
49. Wu, X.; Wang, X.; Chen, X.; Yang, X.; Ma, Q.; Xu, G.; Yu, L.; Ding, J. Injectable and thermosensitive hydrogels mediating a universal macromolecular contrast agent with radiopacity for noninvasive imaging of deep tissues. *Bioact. Mater.* **2021**, *6*, 4717–4728. [[CrossRef](#)] [[PubMed](#)]
50. Dukic, W.; Delija, B.; Derossi, D.; Dacic, I. Radiopacity of composite dental materials using a digital X-ray system. *Dent. Mater. J.* **2012**, *31*, 47–53. [[CrossRef](#)] [[PubMed](#)]
51. Hitij, T.; Fidler, A. Radiopacity of dental restorative materials. *Clin. Oral Investig.* **2013**, *17*, 1167–1177. [[CrossRef](#)] [[PubMed](#)]
52. Fu, N.; Li, A.; Zhang, J.; Zhang, P.; Zhang, H.; Yang, S.; Zhang, J. Liposome-camouflaged iodinated mesoporous silica nanoparticles with high loading capacity, high hemodynamic stability, high biocompatibility and high radiopacity. *Int. J. Pharmaceut.* **2024**, *650*, 123700. [[CrossRef](#)] [[PubMed](#)]
53. Emonde, C.V.; Eggers, M.E.; Wichmann, M.; Hurschler, C.; Ettinger, M.; Denkena, B. Radiopacity Enhancements in Polymeric Implant Biomaterials: A Comprehensive Literature Review. *ACS Biomater. Sci. Eng.* **2024**, *10*, 1323–1334. [[CrossRef](#)] [[PubMed](#)]

Disclaimer/Publisher’s Note: The statements, opinions and data contained in all publications are solely those of the individual author(s) and contributor(s) and not of MDPI and/or the editor(s). MDPI and/or the editor(s) disclaim responsibility for any injury to people or property resulting from any ideas, methods, instructions or products referred to in the content.